



Science Arts & Métiers (SAM)

is an open access repository that collects the work of Arts et Métiers Institute of Technology researchers and makes it freely available over the web where possible.

This is an author-deposited version published in: <https://sam.ensam.eu>
Handle ID: <http://hdl.handle.net/10985/19659>

To cite this version :

Muhammad Waqar NASIR, Hocine CHALAL, Farid ABED-MERAIM - Prediction of forming limits for porous materials using void-size dependent model and bifurcation approach - Meccanica - Vol. 55, n°9, p.1829–1845 - 2020

Any correspondence concerning this service should be sent to the repository

Administrator : scienceouverte@ensam.eu



Prediction of forming limits for porous materials using void-size dependent model and bifurcation approach

Muhammad Waqar Nasir^{1,2, a)} Hocine Chalal^{1, b)} Farid Abed-Meraim^{1, c)}

¹ *Laboratory LEM3, Université de Lorraine, CNRS, Arts et Métiers ParisTech, F-57000 Metz, France.*

² *Department of Mechanical Engineering, University of Engineering and Technology, Lahore 54000, Pakistan.*

^{a)} muhammad_waqar.nasir@ensam.eu

^{b)} Corresponding author: hocine.chalal@ensam.eu

^{c)} farid.abed-meraim@ensam.eu

Abstract

The scientific literature has shown the strong effect of void size on material response. Several yield functions have been developed to incorporate the void size effects in ductile porous materials. Based on the interface stresses of the membrane around a spherical void, a Gurson-type yield function, which includes void size effects, is coupled with the bifurcation theory for the prediction of plastic strain localization. The constitutive equations as well as the bifurcation-based localization criterion are implemented into the finite element code ABAQUS/Standard within the framework of large plastic deformations. The resulting numerical tool is applied to the prediction of forming limit diagrams (FLDs) for an aluminum material. The effect of void size on the prediction of FLDs is investigated. It is shown that smaller void sizes lead to an increase in the ductility limits of the material. This effect on the FLDs becomes more significant for high initial porosity, due to the increase of void-matrix interface strength within the material.

Keywords:

Void size effect; Bifurcation approach; Gurson-type model; Forming limit diagram; Ductile damage; Localized necking

1. Introduction

Sheet metal forming, associated with its wide range of products, is undoubtedly a manufacturing process of great importance involving plastic deformation of sheet metals into a desired shape. For safer design perspective of the manufactured parts, it is desirable that sheet

metal forming processes should not give rise to localized deformations, which as precursor, ultimately lead to material failure. Thus, prediction of localized deformation is of key importance in selecting the forming process parameters. Forming limit diagram (FLD), originally proposed by Keeler & Backofen [1] and Goodwin [2], is a very useful and practical approach for the characterization of ductility limits in sheet metal forming processes. FLD is the plot of in-plane limiting strains, for a sheet metal subjected to biaxial stretching, at the onset of localized necking. Traditionally, FLDs are determined experimentally, using deep drawing tests with various sheet specimen geometries (covering various strain-path ratios), and measuring the in-plane strains at the occurrence of localized necking. However, such experimental determination of FLDs for sheet metals is both costly and time consuming. As an interesting alternative, the development in recent years of constitutive models and material instability criteria for the prediction of plastic strain localization has enabled determining FLDs through numerical simulations.

In addition to the anisotropic plastic behavior of sheet metals, ductile damage, which induces softening, can also be introduced in the constitutive equations, thus providing a more realistic mechanical response for sheet metals. In the past three decades, two damage theories, in this regard, have been developed: Continuum Damage Mechanics (CDM) and micromechanics-based damage theory. The CDM approach treats the damage variable as a scalar or tensor depending upon the softening behavior and anisotropy, as addressed extensively earlier in the literature (see, e.g., [3–14]). As to the micromechanics-based damage approach, the damage variable is taken to describe the void growth in porous materials. The first micromechanics-based damage model, which has been subsequently widely used, was proposed by Gurson [15]. Later, the Gurson model has been modified and extended in various domains and applications. For instance, Gologanu et al. [16-17] extended the Gurson model for oblate and prolate voids, while Madou and Leblond [18-20] and Madou et al. [21] extended the model for non-spheroidal voids. In the works of Dormieux and Kondo [22], Monchiet and Bonnet [23] and Morin et al. [24], variants of the Gurson model have been developed, which take into account the effect of initial void size, while Lacroix et al. [25] and Morin et al. [26] proposed a Gurson-type layer model with isotropic and kinematic hardening.

The widely-used Gurson model for describing the mechanical behavior of porous metallic materials involves only one variable for the analysis of void growth. The original Gurson model does not incorporate the void size in the yield surface. However, this model has been applied to materials with micron void sizes as well as submicron void sizes. Due to the mechanism of dislocation motion, plasticity depends upon internal length scale factor, and when the cavity size is equal to or less than the order of internal length scale, application of the original Gurson model is no more justified (see Hutchinson [27]). It is also well known that higher strength is associated with smaller cavity sizes. This observation, in particular, has found applications in many advanced emerging fields, such as Micro Electro-Mechanical Systems (MEMS). In this context,

it has been shown in the literature that the yield surface is larger as compared to the original Gurson yield surface for void sizes in the range of micron and submicron (see, e.g., Wen et al. [28]). Experimental investigations have also revealed the void size effects on material behavior (see, e.g., [29–38]). Concurrently, several numerical and unit cell studies have equally shown the void size effects (see, e.g., Liu et al. [39], Monchiet and Bonnet [23]). In particular, Molecular-Dynamics analysis performed by Brach et al. [40], for an aluminum single crystal, shows strengthening of the material with the decrease in void radius. Experiments have also shown that, for nano-porous materials, the decrease in void size causes an increase in material strength (see Biener et al. [41-42], Hakamada and Mabuchi [43]). Atomistic simulations performed by Mi et al. [44] showed strong void-size dependency of the stress–strain response and porosity evolution for metallic alloys. They suggested that large void sizes give low values of yield stress as compared to small voids. It has also been found that the porosity evolution for small voids is delayed as compared to large voids before yielding, while it accelerates in plastic regime, causing the rapid decrease in stress carrying capacity for smaller voids as compared to larger voids. They pointed out, through their atomistic simulations, the need for enhancement of the Gurson model to incorporate the void size in the yield function. Their simulations show that, for the same value of initial porosity, smaller voids result in increased material strength. Xu et al. [45-46] investigated experimentally the size effects on material hardening and forming limits, and proposed a constitutive model accounting for void size effects. Their observations have shown that small grain size, and thus small void size, leads to an increase in strain hardening and forming limits. Later, Xu et al. [47] have implemented their size-dependent constitutive model for the optimization of the hydroforming process of sheet metals.

To account for the interface stresses between the nano-voids and the matrix material, Dormieux and Kondo [22] extended the Gurson model to incorporate the void size effect by considering a hypothetical membrane surrounding the voids. A non-dimensional parameter is introduced in the resulting yield function, which depends on the void size and the strength of interface. Dormieux and Kondo [48] and Brach et al. [49] further extended the void-size dependent model for nonlinear behavior of porous materials by applying nonlinear homogenization techniques. Their yield surfaces show the increase in material strength for smaller void sizes.

Parallel to the above-discussed constitutive models, which take into account the void size effect, various instability criteria have been developed in the literature for the prediction of diffuse and localized necking. Considère [50] proposed the maximum force criterion as an indicator of diffuse necking. According to this criterion, instability occurs when the maximum load point is yielded during uniaxial tension. The extension of Considère’s criterion to in-plane biaxial loading has been proposed by Swift [51]. Using the bifurcation approach, Hill [52] presented a material instability criterion for localized necking, namely Hill’s zero-extension criterion. However, this criterion predicts the ductility limit only for the left-hand side of the FLD. For the complete range of strain-path ratios, some authors suggested combining Hill

criterion [52] with Swift criterion [51]. Adopting the maximum force approach, Hora et al. [53] extended the Swift [51] and Considère [50] criteria for localized necking by introducing the effect of strain path. Marciniak and Kuczyński [54] introduced another approach for the prediction of plastic instability, namely the initial imperfection approach, also referred to as the M–K method. The M–K imperfection approach is widely used in many applications for the prediction of localized necking. In another class of theoretical approaches, based on the condition of loss of uniqueness for the solution of the boundary value problem, the general bifurcation criterion was proposed by Hill [55]. Similar to the general bifurcation criterion, the limit point bifurcation condition was proposed by Valanis [56]. Rudnicki and Rice [57] and Rice [58] extended the bifurcation approach in the form of loss of ellipticity condition. According to this criterion, material instability, in the form of plastic strain localization, occurs when the acoustic tensor becomes singular. Similar to Rice [58] bifurcation criterion, Bigoni and Hueckel [59] and Neilsen and Schreyer [60] proposed the condition of loss of strong ellipticity for the prediction of localized necking. Other types of plastic instability criteria have also been developed in the literature, which are based on the analysis of strain and stress evolutions during the loading by using finite element simulations (see, e.g., Volk and Hora [61], Situ et al. [62], Narasimhan and Wagoner [63]).

In the present work, the void-size dependent constitutive model proposed by Dormieux and Kondo [22] is combined with the Rice [58] bifurcation criterion to predict forming limit diagrams of sheet metals. Similar approaches have been followed by Mansouri et al. [64] and Chalal and Abed-Meraim [65], in which the Gurson–Tvergaard–Needleman (GTN) model has been coupled with the Rice bifurcation criterion for the prediction of ductility limits. In the latter studies, the effect of void size on the prediction of FLDs was not considered, which is taken into account in the present contribution. The organization of the paper is as follows. First, the constitutive equations related to the Dormieux and Kondo [22] model and the equations governing the Rice bifurcation criterion are presented. Then, validation of the resulting model and its numerical implementation is conducted using finite element simulations for aluminum alloy Al5754. Finally, numerical results in terms of FLDs obtained with the proposed approach are presented and discussed along with some concluding remarks.

2. Constitutive equations

Dormieux and Kondo [22] extended the original Gurson model by considering a membrane surrounding a spherical void inside a spherical representative volume element (RVE). The membrane around the void is acted on by a surface tension, which produces surface stresses around the voids. The strength of the membrane follows the von Mises criterion, with k_{int} (N/m) being the cavity interface strength. Performing a limit analysis, the yield function has been derived by Dormieux and Kondo [22], which incorporates the void size. The yield function is expressed in the form of parametric equations:

$$\begin{aligned}
\Phi[\Sigma_{\text{eq}}(\xi), \Sigma_{\text{m}}(\xi)] &= 0, \\
3\Sigma_{\text{m}} = \text{tr}(\boldsymbol{\Sigma}) &= \bar{\sigma} \left(2(\sinh^{-1}(\xi) - \sinh^{-1}(f\xi)) + \Gamma \frac{6\xi}{\sqrt{\xi^2 + 3/5}} \right), \\
\Sigma_{\text{eq}} &= \bar{\sigma} \left(\sqrt{1 + f^2\xi^2} - f\sqrt{1 + \xi^2} + \Gamma \frac{9f}{5\sqrt{\xi^2 + 3/5}} \right),
\end{aligned} \tag{1}$$

where $\xi = \frac{2D_{\text{m}}}{f D_{\text{eq}}}$ is a dimensionless parameter defined as a function of the mean part D_{m} and the equivalent part D_{eq} of the macroscopic strain rate tensor \mathbf{D} . In Eq. (1), $\boldsymbol{\Sigma}$ is the Cauchy stress tensor, $\bar{\sigma}$ is the yield stress of the fully dense matrix, f is the void volume fraction, $\Sigma_{\text{eq}} = \sqrt{\frac{3}{2} \boldsymbol{\Sigma}' : \boldsymbol{\Sigma}'}$ is the macroscopic equivalent stress, with $\boldsymbol{\Sigma}'$ and Σ_{m} the deviatoric and hydrostatic part of the Cauchy stress tensor, respectively, and Γ is a non-dimensional parameter, which depends on the void size a and on the cavity interface strength k_{int} as:

$$\Gamma = \frac{k_{\text{int}}}{a\bar{\sigma}}. \tag{2}$$

For illustration purposes, the above parametric yield function is plotted in Fig. 1 for $\Gamma = 0, 0.2$ and 0.43 , along with the original Gurson model (i.e., without void size effect). It is worth noting that the Gurson model is recovered from the Dormieux and Kondo [22] model (D–K model) when $\Gamma = 0$. Note that owing to the symmetry of the parametric yield surface with respect to $\frac{\Sigma_{\text{eq}}}{\bar{\sigma}}$ axis, only the first quadrant is plotted.

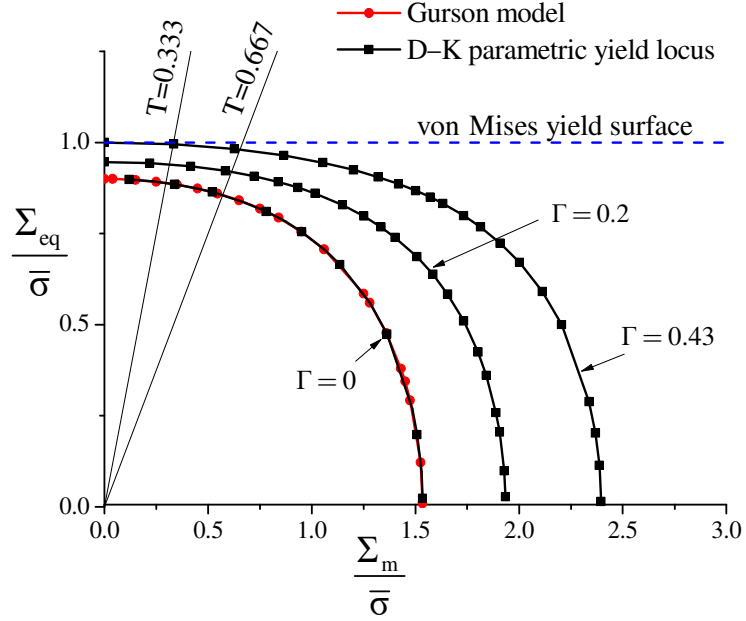


Fig. 1. Parametric yield surface for $f = 0.1$ and $\Gamma = 0, 0.2$ and 0.43 .

From Fig. 1, it can be seen that the yield locus becomes larger for smaller void sizes (i.e., larger values of Γ). As the void size increases (i.e., smaller values of Γ), the size dependency of the D–K model becomes negligible, while for $\Gamma = 0$ (i.e., very large void sizes), the Gurson model is recovered, as shown in Fig. 1. In addition, two linear stress paths, corresponding to constant stress triaxiality of $T = 0.333$ (i.e., uniaxial tension) and $T = 0.667$ (balanced biaxial tension) are highlighted in Fig. 1. Note that, in sheet metal forming applications, the range of stress triaxiality lies typically between 0.333 and 0.667. In this range of stress triaxiality, it can be observed that the parametric yield locus is sensitive to void size.

Morin et al. [24] have numerically implemented the D–K model by using the heuristic extension of Gurson’s model for isotropic hardening. The yield stress $\bar{\sigma}$, which was considered as a constant value in the D–K model (i.e., without hardening), is actually a function of the cumulated equivalent plastic strain $\bar{\epsilon}^p$, which allows modeling isotropic hardening. The following isotropic hardening laws are considered in this work:

$$\begin{aligned} \bar{\sigma}(\bar{\epsilon}^p) &= K(\epsilon_0 + \bar{\epsilon}^p)^n \quad (\text{Swift's hardening law}), \\ \bar{\sigma}(\bar{\epsilon}^p) &= \bar{\sigma}_0 \left(1 + \frac{\bar{\epsilon}^p}{\bar{\sigma}_0 / E} \right)^n \quad (\text{Power hardening law}), \end{aligned} \quad (3)$$

where K , ϵ_0 and n are hardening parameters, while $\bar{\sigma}_0$ and E denote respectively the initial yield stress and Young’s modulus. From the equivalence principle of the plastic work rate, the equivalent plastic strain rate $\dot{\bar{\epsilon}}^p$ and the macroscopic plastic strain rate tensor \mathbf{D}^p are related as:

$$(1-f)\bar{\sigma}\dot{\bar{\epsilon}}^p = \boldsymbol{\Sigma} : \mathbf{D}^p. \quad (4)$$

Morin et al. [24] have implemented into the D–K model the evolution of the porosity due to growth, based on the matrix incompressibility (see, e.g., Tvergaard, [66]):

$$\dot{f} = \dot{f}_g = (1-f)\text{tr}(\mathbf{D}^p). \quad (5)$$

The evolution of the void size (i.e., \dot{a}) has been modeled by Morin et al. [24], by considering that for a spherical void of volume ω , present inside a spherical RVE of volume Ω , the volume constancy of the matrix material implies that $\dot{\omega} = \dot{\Omega}$. As the porosity is defined by $f = \frac{\omega}{\Omega}$, the evolution equation for the porosity and thus for the void size writes:

$$\begin{aligned} \dot{f} &= \frac{d}{dt} \left(\frac{\omega}{\Omega} \right) = \frac{\Omega\dot{\omega} - \omega\dot{\Omega}}{\Omega^2} = \frac{\dot{\omega}}{\omega} \left(\frac{\omega}{\Omega} - \frac{\omega^2\dot{\Omega}}{\Omega^2\dot{\omega}} \right) = 3\frac{\dot{a}}{a}(f - f^2), \\ \dot{a} &= \frac{a}{3f(1-f)} \dot{f}. \end{aligned} \quad (6)$$

Using the definition of the Γ parameter, its time derivative can be expressed as:

$$\dot{\Gamma} = \frac{d}{dt} \left(\frac{k_{\text{int}}}{a\bar{\sigma}} \right) = \frac{-k_{\text{int}}}{(a\bar{\sigma})^2} (a\dot{\bar{\sigma}} + \dot{a}\bar{\sigma}). \quad (7)$$

The time derivative of the yield stress (i.e., $\dot{\bar{\sigma}}$) can be evaluated as:

$$\dot{\bar{\sigma}} = \frac{\partial \bar{\sigma}}{\partial \bar{\epsilon}^p} \dot{\bar{\epsilon}}^p = h(\bar{\epsilon}^p) \dot{\bar{\epsilon}}^p, \quad (8)$$

where $h(\bar{\epsilon}^p)$ is the hardening slope of the material, which depends on the selected isotropic hardening law.

To determine the elastic–plastic tangent modulus, the plastic multiplier $\dot{\gamma}$ and the yield function Φ can be combined in the form of the following Kuhn–Tucker relation:

$$\Phi \leq 0, \quad \dot{\gamma} \geq 0, \quad \Phi \dot{\gamma} = 0. \quad (9)$$

The above expression shows that no plastic flow occurs (i.e., $\dot{\gamma} = 0$) when $\Phi < 0$, while a strict plastic loading (i.e., $\dot{\gamma} > 0$) necessarily implies $\dot{\Phi} = 0$. The latter condition, called consistency condition, is used to derive the elastic–plastic tangent modulus as follows:

$$\dot{\Phi}(\boldsymbol{\Sigma}, f, \Gamma, \bar{\sigma}) = \mathbf{V}_{\boldsymbol{\Sigma}} : \dot{\boldsymbol{\Sigma}} + \mathbf{V}_{\bar{\sigma}} \dot{\bar{\sigma}} + \mathbf{V}_{\Gamma} \dot{\Gamma} + \mathbf{V}_f \dot{f} = 0, \quad (10)$$

where $\mathbf{V}_{\boldsymbol{\Sigma}}, \mathbf{V}_{\bar{\sigma}}, \mathbf{V}_{\Gamma}$ and \mathbf{V}_f are the partial derivatives of the yield function Φ with respect to $\boldsymbol{\Sigma}, \bar{\sigma}, \Gamma$ and f , respectively. Their expressions are derived as follows:

$$\mathbf{V}_{\boldsymbol{\Sigma}} = \frac{\partial \Phi}{\partial \boldsymbol{\Sigma}} = \frac{\partial \Phi}{\partial \Sigma_m} \frac{\partial \Sigma_m}{\partial \boldsymbol{\Sigma}} + \frac{\partial \Phi}{\partial \Sigma_{eq}} \frac{\partial \Sigma_{eq}}{\partial \boldsymbol{\Sigma}}, \quad (11)$$

where

$$\begin{aligned} \frac{\partial \Phi}{\partial \Sigma_m} &= -C^2 \frac{d\Sigma_{eq}}{d\xi}, \\ \frac{\partial \Phi}{\partial \Sigma_{eq}} &= C^2 \frac{d\Sigma_m}{d\xi}, \end{aligned} \quad (12)$$

with C a real constant, which depends on ξ . By using Eq. (12), $\mathbf{V}_{\boldsymbol{\Sigma}}$ can be expressed as:

$$\mathbf{V}_{\boldsymbol{\Sigma}} = -C^2 \frac{d\Sigma_{eq}}{d\xi} \frac{\partial \Sigma_m}{\partial \boldsymbol{\Sigma}} + C^2 \frac{d\Sigma_m}{d\xi} \frac{\partial \Sigma_{eq}}{\partial \boldsymbol{\Sigma}}. \quad (13)$$

By taking the derivative of Eq. (1) with respect to parameter ξ , we obtain:

$$\begin{aligned} \frac{d\Sigma_{eq}}{d\xi} &= \bar{\sigma} \left\{ \frac{f^2 \xi}{\sqrt{1+f^2 \xi^2}} - \frac{f \xi}{\sqrt{1+\xi^2}} - \frac{9f \Gamma \xi}{5} \left(\xi^2 + \frac{3}{5} \right)^{-\frac{3}{2}} \right\}, \\ \frac{d\Sigma_m}{d\xi} &= \frac{\bar{\sigma}}{3} \left\{ 2 \left[\frac{1}{\sqrt{1+\xi^2}} - \frac{f}{\sqrt{1+f^2 \xi^2}} \right] + 6\Gamma \left[-\xi^2 \left(\xi^2 + \frac{3}{5} \right)^{-\frac{3}{2}} + \left(\xi^2 + \frac{3}{5} \right)^{-\frac{1}{2}} \right] \right\}. \end{aligned} \quad (14)$$

The remaining partial derivatives in Eq. (11) write:

$$\begin{aligned} \frac{\partial \Sigma_m}{\partial \boldsymbol{\Sigma}} &= \frac{1}{3} \mathbf{1}, \\ \frac{\partial \Sigma_{eq}}{\partial \boldsymbol{\Sigma}} &= \frac{3}{2} \frac{\boldsymbol{\Sigma}'}{\Sigma_{eq}}, \end{aligned} \quad (15)$$

where $\mathbf{1}$ is the second-order identity tensor. Finally, $\mathbf{V}_{\boldsymbol{\Sigma}}$ in Eq. (13) writes:

$$\mathbf{V}_\Sigma = \mathbf{C}^2 \left\{ -\frac{d\Sigma_{\text{eq}}}{d\xi} \frac{1}{3} \mathbf{1} + \frac{d\Sigma_m}{d\xi} \frac{3}{2} \frac{\Sigma'}{\Sigma_{\text{eq}}} \right\} = \mathbf{C}^2 \mathbf{V}_{\Sigma_N}. \quad (16)$$

By following similar steps, the general expressions of the partial derivatives $\mathbf{V}_{\bar{\sigma}}$, \mathbf{V}_Γ and \mathbf{V}_f can be obtained as follows:

$$\begin{aligned} \mathbf{V}_{\bar{\sigma}} &= \frac{\partial \Phi}{\partial \bar{\sigma}} = \frac{\partial \Phi}{\partial \Sigma_m} \frac{\partial \Sigma_m}{\partial \bar{\sigma}} + \frac{\partial \Phi}{\partial \Sigma_{\text{eq}}} \frac{\partial \Sigma_{\text{eq}}}{\partial \bar{\sigma}}, \\ \mathbf{V}_f &= \frac{\partial \Phi}{\partial f} = \frac{\partial \Phi}{\partial \Sigma_m} \frac{\partial \Sigma_m}{\partial f} + \frac{\partial \Phi}{\partial \Sigma_{\text{eq}}} \frac{\partial \Sigma_{\text{eq}}}{\partial f}, \\ \mathbf{V}_\Gamma &= \frac{\partial \Phi}{\partial \Gamma} = \frac{\partial \Phi}{\partial \Sigma_m} \frac{\partial \Sigma_m}{\partial \Gamma} + \frac{\partial \Phi}{\partial \Sigma_{\text{eq}}} \frac{\partial \Sigma_{\text{eq}}}{\partial \Gamma}, \end{aligned} \quad (17)$$

and more specifically:

$$\begin{aligned} \mathbf{V}_{\bar{\sigma}} &= \mathbf{C}^2 \left\{ -\frac{d\Sigma_{\text{eq}}}{d\xi} \frac{\partial \Sigma_m}{\partial \bar{\sigma}} + \frac{d\Sigma_m}{d\xi} \frac{\partial \Sigma_{\text{eq}}}{\partial \bar{\sigma}} \right\} = \mathbf{C}^2 \mathbf{V}_{\bar{\sigma}_N}, \\ \mathbf{V}_f &= \mathbf{C}^2 \left\{ -\frac{d\Sigma_{\text{eq}}}{d\xi} \frac{\partial \Sigma_m}{\partial f} + \frac{d\Sigma_m}{d\xi} \frac{\partial \Sigma_{\text{eq}}}{\partial f} \right\} = \mathbf{C}^2 \mathbf{V}_{f_N}, \\ \mathbf{V}_\Gamma &= \mathbf{C}^2 \left\{ -\frac{d\Sigma_{\text{eq}}}{d\xi} \frac{\partial \Sigma_m}{\partial \Gamma} + \frac{d\Sigma_m}{d\xi} \frac{\partial \Sigma_{\text{eq}}}{\partial \Gamma} \right\} = \mathbf{C}^2 \mathbf{V}_{\Gamma_N}. \end{aligned} \quad (18)$$

The macroscopic plastic strain rate tensor \mathbf{D}^p is defined using the following classical plastic flow rule (normality law):

$$\mathbf{D}^p = \dot{\gamma} \mathbf{V}_\Sigma. \quad (19)$$

Substituting Eq. (16) in the above equation, the macroscopic plastic strain rate tensor becomes:

$$\mathbf{D}^p = \dot{\gamma} \mathbf{C}^2 \mathbf{V}_{\Sigma_N} = \dot{\gamma}_N \mathbf{V}_{\Sigma_N}, \quad (20)$$

where

$$\dot{\gamma}_N = \dot{\gamma} \mathbf{C}^2. \quad (21)$$

The macroscopic Cauchy stress rate tensor is expressed, in the co-rotational material frame, by the following hypoelastic law:

$$\dot{\Sigma} = \mathbf{C}^e : (\mathbf{D} - \mathbf{D}^p) = \mathbf{C}^{\text{ep}} : \mathbf{D}, \quad (22)$$

where \mathbf{D} is the macroscopic strain rate tensor, \mathbf{C}^e is the fourth-order tensor of elasticity constants, and \mathbf{C}^{ep} is the elastic–plastic tangent modulus, which needs to be determined. By using all of the above-described partial derivatives of the yield function, and considering Eqs. (20) and (22), the consistency condition (10) can be developed as follows:

$$\mathbf{V}_{\Sigma_N} : \mathbf{C}^e : \mathbf{D} - \dot{\gamma}_N \mathbf{V}_{\Sigma_N} : \mathbf{C}^e : \mathbf{V}_{\Sigma_N} + \mathbf{V}_{\bar{\sigma}_N} \dot{\bar{\sigma}} + \mathbf{V}_{\Gamma_N} \dot{\Gamma} + \mathbf{V}_{f_N} \dot{f} = 0. \quad (23)$$

Then, substituting Eqs. (4-8) and (20) into the above consistency condition, the expression of the plastic multiplier is derived as follows:

$$\dot{\gamma}_N = \frac{\mathbf{V}_{\Sigma_N} : \mathbf{C}^e : \mathbf{D}}{H_\gamma}, \quad (24)$$

where

$$H_\gamma = \mathbf{V}_{\Sigma_N} : \mathbf{C}^e : \mathbf{V}_{\Sigma_N} - h \frac{\Sigma : \mathbf{V}_{\Sigma_N}}{(1-f)\bar{\sigma}} \left\{ \mathbf{V}_{\bar{\sigma}_N} - \mathbf{V}_{\Gamma_N} \frac{k_{int}}{a\bar{\sigma}^2} \right\} - (1-f)(\mathbf{V}_{\Sigma_N} : \mathbf{1}) \left\{ \mathbf{V}_{f_N} - \frac{k_{int} \mathbf{V}_{\Gamma_N}}{3f(1-f)a\bar{\sigma}} \right\}. \quad (25)$$

Finally, the elastic–plastic tangent modulus is derived as:

$$\mathbf{C}^{ep} = \mathbf{C}^e - \frac{(\mathbf{C}^e : \mathbf{V}_{\Sigma_N}) \otimes (\mathbf{V}_{\Sigma_N} : \mathbf{C}^e)}{H_\gamma}. \quad (26)$$

2.1 Material objectivity

The constitutive equations described above are implemented into the finite element code ABAQUS/Standard in the framework of large strains. To achieve this, objective derivatives for the tensor variables must be used to ensure the material objectivity (i.e., frame invariance of the constitutive model). A convenient way to maintain the material objectivity is to reformulate the tensor variables in terms of their rotation compensated counterparts. More specifically, if \mathbf{A} and \mathbf{B} represent a second- and a fourth-order tensor, respectively, their associated rotation compensated expressions can be calculated as:

$$\widehat{\mathbf{A}}_{ij} = \mathbf{R}_{ki} \mathbf{R}_{lj} \mathbf{A}_{kl} \quad \text{and} \quad \widehat{\mathbf{B}}_{ijkl} = \mathbf{R}_{pi} \mathbf{R}_{qj} \mathbf{R}_{rk} \mathbf{R}_{sl} \mathbf{B}_{pqrs}, \quad (27)$$

where \mathbf{R} is a rotation matrix, which is defined using the following rate equation:

$$\dot{\mathbf{R}} \cdot \mathbf{R}^T = \boldsymbol{\Omega}, \quad (28)$$

where $\boldsymbol{\Omega}$ is the skew-symmetric spin tensor. Different objective rates of the Cauchy stress tensor are available in the literature. Among them, the well-known Jaumann stress rate, Green–Naghdi stress rate, and Truesdell stress rate. In the present contribution, Jaumann objective rates are considered for the constitutive equations, which is consistent with the procedure used in the

finite element software ABAQUS/Standard. The Jaumann objective stress rate $\dot{\Sigma}^J$ is expressed as:

$$\dot{\Sigma}^J = \dot{\Sigma} - \Omega \cdot \Sigma + \Sigma \cdot \Omega. \quad (29)$$

2.2 Bifurcation approach

In the present study, the strain localization criterion proposed by Rudnicki and Rice [57] and Rice [58] is combined with the D–K model to predict the ductility limits of sheet metals. This criterion is based on the bifurcation theory, which predicts the occurrence of strain localization in the form of infinite planar band defined by its normal \mathbf{n} (see Fig. 2). The equilibrium conditions along the localization band, which express the continuity of the nominal stress rate vector across the discontinuity surfaces, can be written as:

$$\mathbf{n} \cdot \llbracket \dot{\mathbf{N}} \rrbracket = \mathbf{0}, \quad (30)$$

where $\llbracket \dot{\mathbf{N}} \rrbracket = \dot{\mathbf{N}}^+ - \dot{\mathbf{N}}^-$ denotes the jump in the nominal stress rate across the localization band planes.

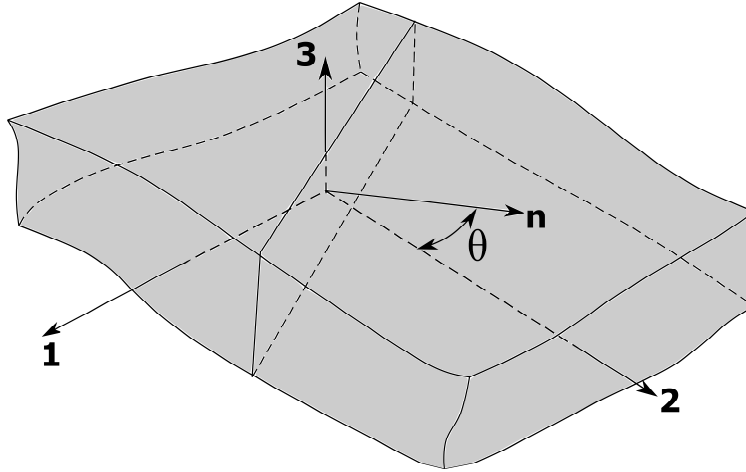


Fig. 2. Schematic illustration of localization band in the plane of sheet metal.

Maxwell's compatibility equation allows expressing the jump in the velocity gradient \mathbf{G} across the localization band as:

$$\llbracket \mathbf{G} \rrbracket = \dot{\mathbf{m}} \otimes \mathbf{n}, \quad (31)$$

where the vector $\dot{\mathbf{m}} = \llbracket \mathbf{G} \rrbracket \cdot \mathbf{n}$ is the jump amplitude vector, which characterizes the mode of localization (e.g., shear bifurcation mode when $\dot{\mathbf{m}} \perp \mathbf{n}$).

On the other hand, the nominal stress rate tensor $\dot{\mathbf{N}}$ is related to the velocity gradient \mathbf{G} by the following expression:

$$\dot{\mathbf{N}} = \mathbf{L} : \mathbf{G}, \quad (32)$$

where \mathbf{L} is the corresponding tangent modulus that needs to be determined. By combining Eqs. (30-32), the critical condition, which corresponds to the loss of ellipticity for the boundary value problem, can be expressed as the singularity of the acoustic tensor $\mathbf{Q} = \mathbf{n} \cdot \mathbf{L} \cdot \mathbf{n}$:

$$\det(\mathbf{Q}) = \det(\mathbf{n} \cdot \mathbf{L} \cdot \mathbf{n}) = 0. \quad (33)$$

As for the sake of material objectivity, Jaumann stress rate has been used in the present work. Within the framework of an updated Lagrangian approach, the expression of the nominal stress rate tensor is given by:

$$\dot{\mathbf{N}} = \dot{\boldsymbol{\Sigma}} + \text{tr}(\mathbf{D})\boldsymbol{\Sigma} - \mathbf{D} \cdot \boldsymbol{\Sigma} - \boldsymbol{\Omega} \cdot \boldsymbol{\Sigma}. \quad (34)$$

Finally, by combining the above equations, the complete expression of the tangent modulus \mathbf{L} is given by:

$$\mathbf{L} = \mathbf{C}^{\text{ep}} + \mathbf{C}_1 - \mathbf{C}_2 - \mathbf{C}_3, \quad (35)$$

where \mathbf{C}_1 , \mathbf{C}_2 and \mathbf{C}_3 are fourth-order tensors, whose expressions are only function of the Cauchy stress components. Their expressions are:

$$\begin{aligned} C_{1ijkl} &= \Sigma_{ij} \delta_{kl}, \\ C_{2ijkl} &= \frac{1}{2} (\Sigma_{jk} \delta_{il} + \Sigma_{jl} \delta_{ik}), \\ C_{3ijkl} &= \frac{1}{2} (\Sigma_{ik} \delta_{jl} - \Sigma_{il} \delta_{jk}), \end{aligned} \quad (36)$$

where δ_{ij} is the kronecker symbol, which is equal to 1 when $i = j$, and to 0 otherwise.

It is worth noting that the present work is dedicated to the prediction of localized necking in thin sheet metals. Although the constitutive equations presented in the previous section are formulated in the fully three-dimensional framework, the Rice bifurcation criterion is derived in this work in the framework of plane-stress conditions. To achieve this, the nominal stress rate tensor, defined by Eq. (32), is rewritten within the framework of plane-stress theory as follows:

$$\dot{\mathbf{N}}_{\alpha\beta} = \mathbf{L}_{\alpha\beta\gamma\delta}^{\text{PS}} \mathbf{G}_{\gamma\delta}, \text{ with } \alpha, \beta, \gamma, \delta = 1, 2, \quad (37)$$

where the expression of the plane-stress tangent modulus \mathbf{L}^{PS} is deduced from the three-dimensional tangent modulus \mathbf{L} using the following relationship:

$$\mathbf{L}_{\alpha\beta\gamma\delta}^{\text{PS}} = \mathbf{L}_{\alpha\beta\gamma\delta} - \mathbf{L}_{\alpha\beta 33} \frac{\mathbf{L}_{33\gamma\delta}}{\mathbf{L}_{3333}}. \quad (38)$$

Note that, within the plane-stress framework, the emergence of the localization band is searched for in the plane of the sheet, with a variation of the band orientation angle θ (see Fig.

(2)) from 0° to 180° . Localized necking is said to occur when the minimum value, over all possible band orientations, of the determinant of the acoustic tensor (see Eq. (33)) becomes zero. The corresponding in-plane strains are considered as the critical strains at localization, which will be used for the FLD plot.

3. Numerical implementation of the D–K model and validation

3.1 Time integration scheme and finite element implementation

The constitutive equations described above have been implemented into the finite element code ABAQUS/Standard in the framework of large strains and three-dimensional approach. In order to reproduce a homogeneous strain state prior to localization, a single finite element with one integration point (specifically, C3D8R solid element in ABAQUS) is used in the simulations, which is subjected to various linear strain paths that are those typically applied to sheet metals under in-plane biaxial stretching. The main motivation behind this choice of loading configuration is to predict plastic instability that is inherent to the ‘material’ alone, with no interference with structural (geometric) effects. The geometry of the single finite element along with the applied boundary conditions are illustrated in Fig. 3. Directions 1 and 2 represent the major and the minor directions, respectively. The linear strain paths are obtained by varying the strain-path ratio from -0.5 , for uniaxial tension, to 1 for balanced biaxial tension. For each loading increment, the stress state is updated using a predictor-corrector approach, following the numerical procedure proposed by Morin et al. [24]. The resulting numerical algorithm is detailed in Table 1. As to the numerical implementation of the Rice bifurcation criterion, the condition of loss of ellipticity, given by Eq. (33), is assessed by computing the determinant of the acoustic tensor for each loading increment and each orientation for the localization band. The numerical detection of the occurrence of localized necking is achieved when the minimum of the acoustic tensor determinant, over all possible orientations for the normal \mathbf{n} to the localization band, becomes non-positive. This procedure is repeated for different strain-path ratios ranging from uniaxial tension to balanced biaxial tension. Then, the corresponding in-plane critical strains are plotted in terms of FLD.

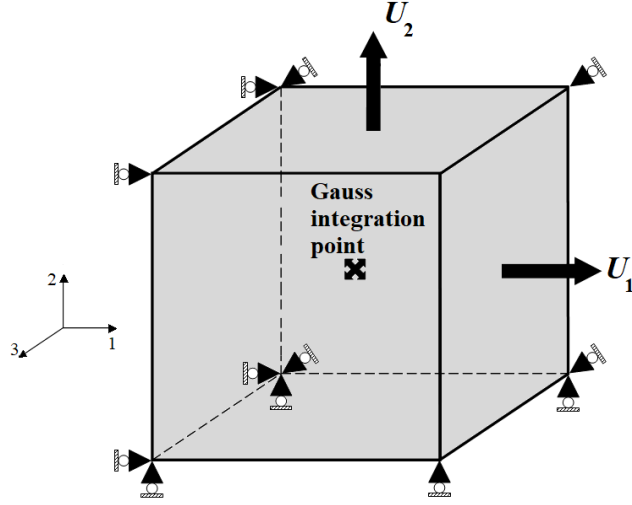


Fig. 3. Boundary conditions for single finite element (C3D8R) subjected to in-plane biaxial stretching.

Table 1

Outline of the predictor-corrector algorithm and time integration scheme.

For $t=0$, initialization of all state variables ($\Sigma = \mathbf{0}$, $\bar{\epsilon}^p = 0$, $\bar{\sigma} = \bar{\sigma}_0$, $f = f_0$, $\mathbf{a} = \mathbf{a}_0$)

Compute elastic predictor $\Sigma_{n+1}^{\text{elast}} = \Sigma_n + \mathbf{C}^e : \Delta \epsilon_{n+1}$

Determine the parameter ξ_{n+1} by solving the nonlinear equation $T(\xi_{n+1}, f_n, \Gamma_n) - T_{n+1}^{\text{elast}} = 0$, in which T is the triaxiality (i.e., $T = \frac{\Sigma_m}{\Sigma_{\text{eq}}}$)

Compute $F = \left[\left(\Sigma_m^{\text{elast}} \right)_{n+1}^2 + \left(\Sigma_{\text{eq}}^{\text{elast}} \right)_{n+1}^2 \right] - \left[\left(\Sigma_m(\xi_{n+1}) \right)_{n+1}^2 + \left(\Sigma_{\text{eq}}(\xi_{n+1}) \right)_{n+1}^2 \right]$

Plastic yield condition:

- If $F < 0$ then (elastic loading)

$$\Sigma_{n+1} = \Sigma_{n+1}^{\text{elast}}, \Delta \bar{\epsilon}^p = 0, \Delta \bar{\sigma} = 0, \Delta f = 0 \text{ and } \Delta \Gamma = 0$$

$$\text{Tangent modulus } \mathbf{C}^{\text{ep}} = \mathbf{C}^e$$

- Else (plastic loading)

Compute $\Delta \gamma_{N,n}$ and ξ_{n+1} using the plastic correction

Compute the corrected Σ_{n+1}

Update the internal variables $\bar{\epsilon}_{n+1}^p$, $\bar{\sigma}_{n+1}$, f_{n+1} and Γ_{n+1}

$$\text{Compute the tangent modulus } \mathbf{C}^{\text{ep}} = \mathbf{C}^e - \frac{(\mathbf{C}^e : \mathbf{V}_{\Sigma_N}) \otimes (\mathbf{V}_{\Sigma_N} : \mathbf{C}^e)}{H\gamma}$$

- End if

Return Σ_{n+1} and \mathbf{C}^{ep} to ABAQUS for solving the equilibrium equations.

3.2 Numerical validation of the D–K model

The above numerical algorithm for the time integration of the constitutive equations of the D–K model has been implemented into the finite element software ABAQUS/Standard via a user-defined material (UMAT) subroutine. This section is devoted to the validation of the numerical implementation of the D–K model. To this end, simulations of the response of an RVE, which is subjected to constant stress triaxialities, are performed with the developed D–K UMAT subroutine and compared with the results provided by Morin et al. [24]. The power-hardening law, as given by Eq. (3), is used for the description of isotropic hardening. The material parameters used in the simulations are summarized in Table 2 (see Morin et al. [24]). Note that the RVE is subjected to two constant stress triaxialities (i.e., $T=1$ and $T=3$). The numerical results in terms of normalized equivalent stress and porosity with respect to equivalent strain, obtained with the present UMAT subroutine, are shown in Figs. 4–7 along with the reference results provided by Morin et al. [24].

Table 2

Material parameters used in the simulations.

E (GPa)	ν	$\bar{\sigma}_0$ (MPa)	n	f_0	k_{int} (N/m)	Γ_0
200	0.3	400	0.1	[0.01, 0.001]	1	[0., 0.5, 1.25, 2.5]

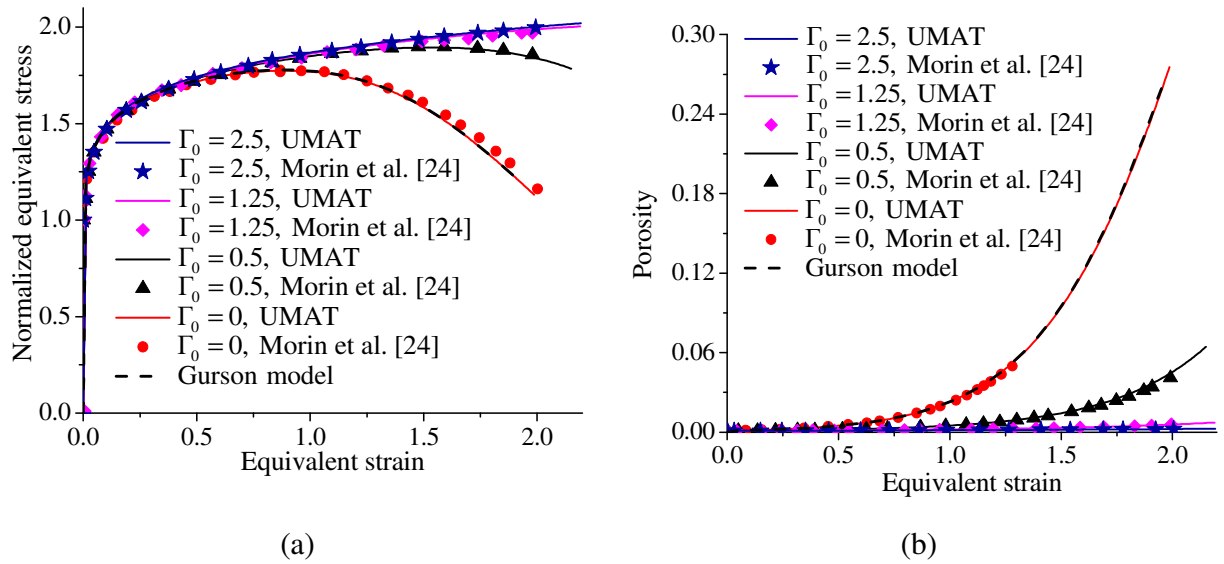


Fig. 4. Evolution of: (a) normalized equivalent stress, and (b) porosity, for stress triaxiality $T=1$ and initial porosity $f_0 = 0.001$.

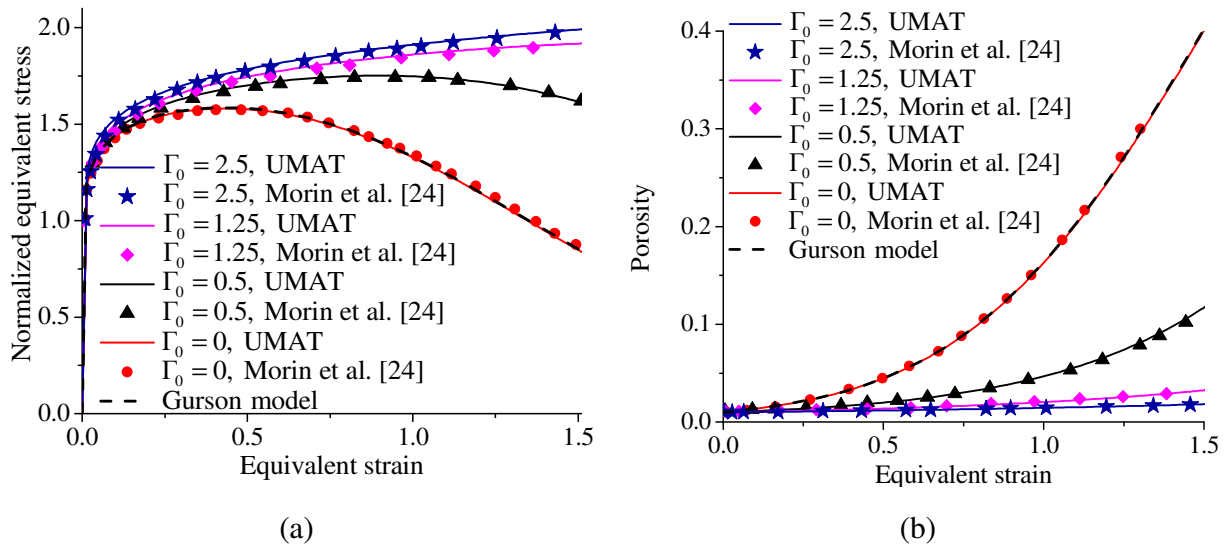


Fig. 5. Evolution of: (a) normalized equivalent stress, and (b) porosity, for stress triaxiality $T=1$ and initial porosity $f_0 = 0.01$.

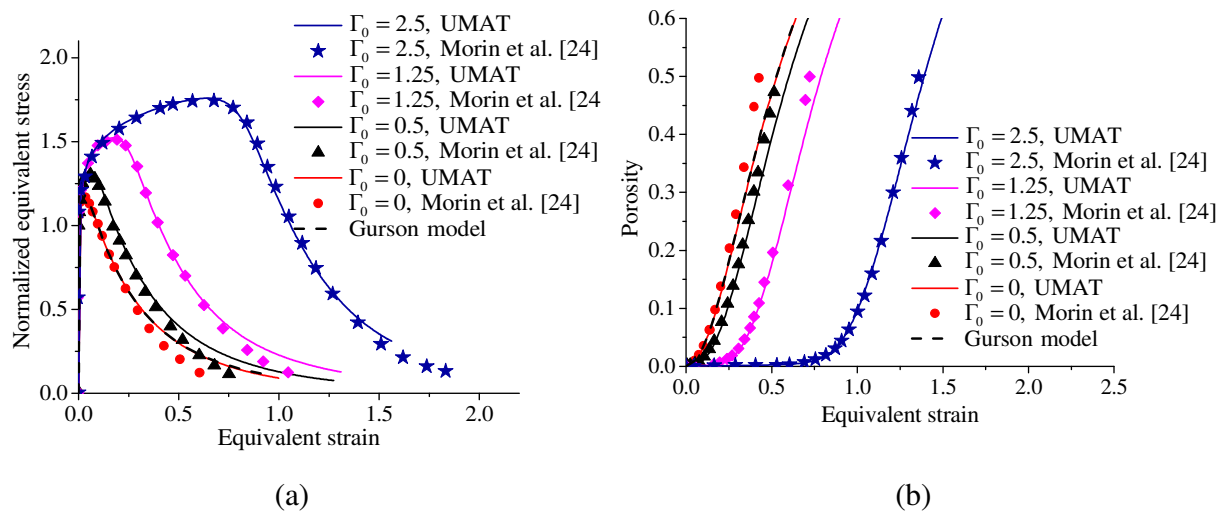


Fig. 6. Evolution of: (a) normalized equivalent stress, and (b) porosity, for stress triaxiality $T=3$ and initial porosity $f_0 = 0.001$.

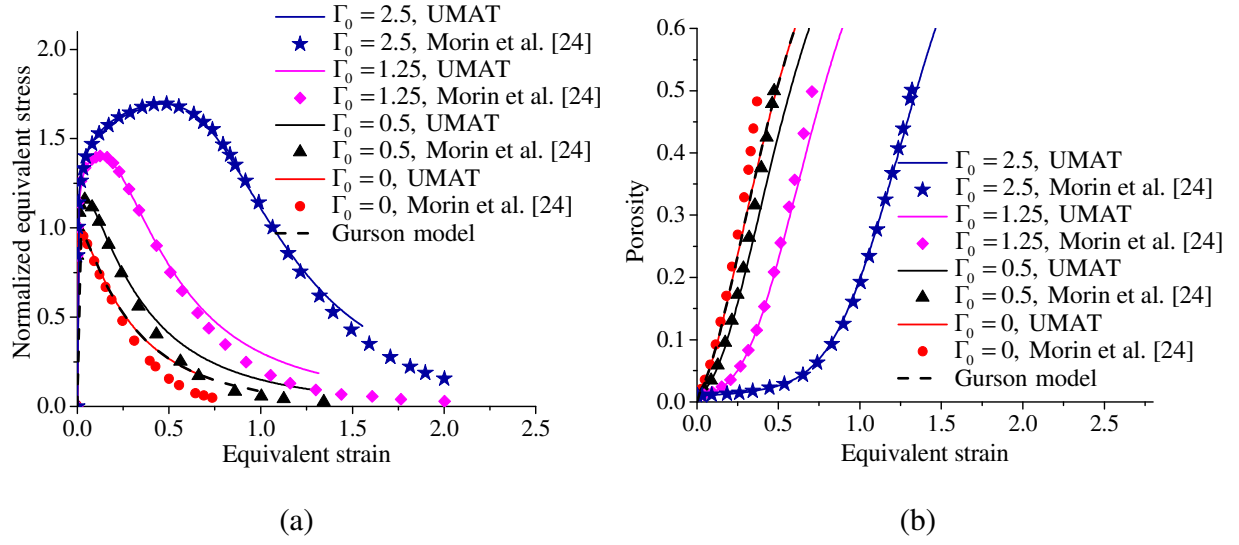


Fig. 7. Evolution of: (a) normalized equivalent stress, and (b) porosity, for stress triaxiality $T=3$ and initial porosity $f_0 = 0.01$.

It is recalled here that the original Gurson model is recovered from the D–K model when $\Gamma_0 = 0$. In this case, the numerical results obtained with the present UMAT subroutine can be compared with those predicted by the Gurson model, which is available in ABAQUS/Standard. When the void-size independent model is considered (i.e., D–K model with $\Gamma_0 = 0$), all the results predicted using the developed UMAT subroutine coincide with their counterparts obtained with the Gurson model, which is fully consistent. As to the case of void-size dependent model (i.e., D–K model with $\Gamma_0 \neq 0$), it can be observed a significant difference between the results predicted by the Gurson model and those provided by the D–K model, which includes the void size effect. More specifically, for small initial porosity and moderate stress triaxiality (i.e., $f_0 = 0.001$ and $T=1$, respectively), a softening regime is predicted by the Gurson model, starting from an equivalent strain of about 1, while no softening regime is shown by the D–K model for high values of Γ_0 (i.e., from $\Gamma_0 = 1.25$ and more in this case, see Fig. 4a). However, stress softening is observed for small values of Γ_0 , which is due to the rapid evolution of the porosity in this range of small initial non-dimensional parameter Γ_0 (see Fig. 4b). For moderate initial porosity as well as high stress triaxiality (i.e., $f_0 = 0.01$ and $T=3$, respectively), the developed UMAT subroutine for the D–K model predicts the same trends as above for both stress and porosity evolutions, which are consistent with the reference predictions provided by Morin et al. [24].

4. Prediction of FLDs with the D–K model and bifurcation analysis

In this section, the resulting coupling between the D–K model and the Rice bifurcation criterion is applied for the prediction of FLDs for Al5754 aluminum material. The associated material parameters used in the simulations are taken from Mansouri et al. [64], as reported in Table 3. The additional parameter Γ_0 , which incorporates the void size effect is varied here to analyze its effect on the prediction of localized necking.

Table 3
Material parameters for the Al5754 aluminum material.

Elastic properties		Swift’s hardening parameters			Initial porosity
E (GPa)	ν	K	ϵ_0	n	f_0
70	0.33	309.1	0.00173	0.177	0.001

The FLDs predicted with the Rice bifurcation criterion are presented in Fig. 8a for the Al5754 aluminum material for three values of the initial non-dimensional parameter (i.e., $\Gamma_0 = 0, 1.5$ and 2.5). It is worth recalling that the original Gurson model, which only describes the elastic–plastic behavior with damage due to porosity growth, can be recovered from the D–K model when $\Gamma_0 = 0$. Therefore, for comparison purposes, the FLD predicted with the original Gurson model and the Rice bifurcation criterion is also presented in Fig. 8a. From this figure, it can be seen that the effect of the initial non-dimensional parameter on strain localization is not perceptible when only the void growth mechanism is considered in the D–K model. Moreover, strain localization does not occur in the right-hand side of the FLD (i.e., for positive biaxial strain-path ratios) due to the low values of porosity in this range of strain paths (i.e., right-hand side of FLD, see Fig. 8b). Indeed, in the works of Mansouri et al. [64] and Chalal and Abed-Meraim [65], it has been shown that, using the bifurcation theory coupled with Gurson-type models, the occurrence of strain localization for positive biaxial strain-path ratios requires the critical hardening modulus to be strongly negative.

In order to further investigate the insensitivity of the strain localization predictions to the different values of the initial non-dimensional parameter (see Fig. 8a), the yield surface for Al5754 is illustrated in Fig. 9. In addition, two linear stress paths, corresponding to the extreme left (uniaxial tension) and right (balanced biaxial tension) strain paths of FLD, i.e. constant stress triaxialities of $T = 0.333$ and $T = 0.667$, respectively, are highlighted in this Fig. 9. Note that, within this narrow range of stress triaxiality ratio, the yield surface points corresponding to different values of initial non-dimensional parameter are almost indistinguishable, which explains the insensitivity of the predicted FLDs to the initial non-dimensional parameter, as observed in Fig. 8a.

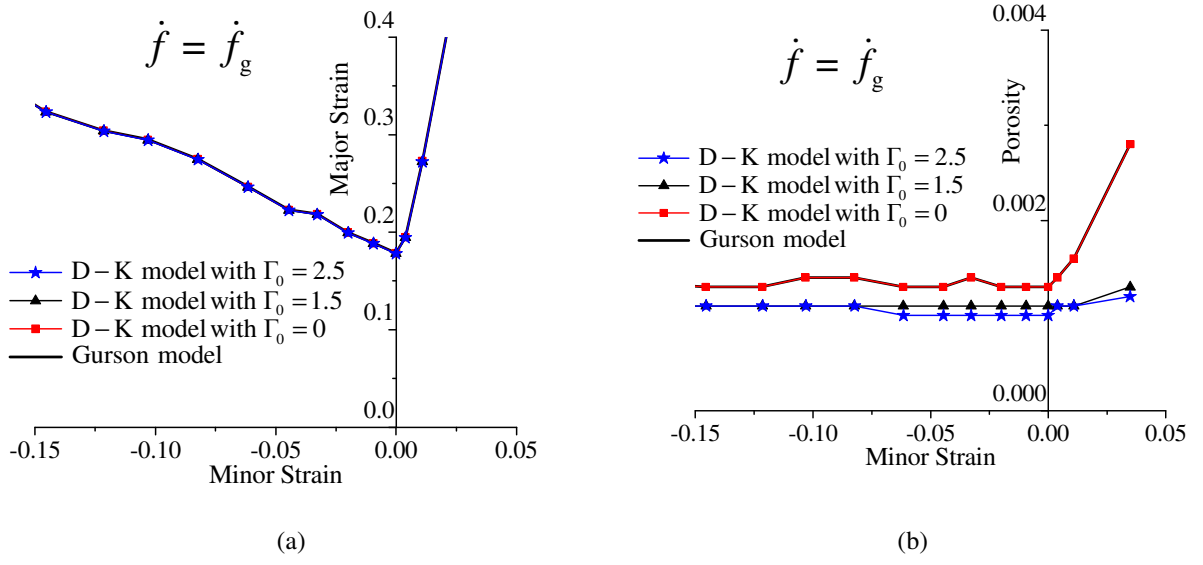


Fig. 8. (a) FLDs, and (b) porosity at localization, for Al5754 aluminum.

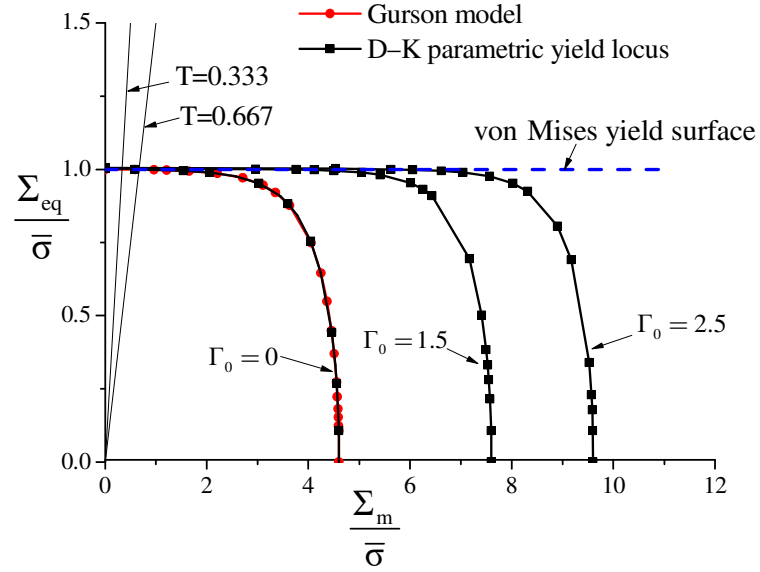


Fig. 9. Parametric yield surface for Al5754 aluminum and $\Gamma_0 = 0, 1.5$ and 2.5 .

To better highlight the effect of the void size on strain localization, nucleation of new voids is considered in what follows, in addition to the void growth mechanism, for both the D–K model and the Gurson model. Accordingly, the evolution of porosity, with an initial value of f_0 , is due to void nucleation and growth, and the porosity rate can then be partitioned as follows:

$$\dot{f} = \dot{f}_g + \dot{f}_n, \quad (39)$$

where \dot{f}_n represents the contribution to the porosity rate from nucleation. The latter is considered to be strain-controlled following the normal distribution relationship proposed by Chu and Needleman [67]:

$$\dot{f}_n = \frac{f_N}{s_N \sqrt{2\pi}} \exp\left(-\frac{1}{2} \left(\frac{\bar{\varepsilon}^p - \varepsilon_N}{s_N}\right)^2\right) \dot{\varepsilon}^p, \quad (40)$$

where f_N , s_N and ε_N are the nucleation parameters. The latter are reported in Table 4 for the Al5754 aluminum material. The corresponding FLDs are presented in Fig. 10a, for which the porosity evolution due to nucleation and growth is considered.

Table 4
Nucleation parameters for the Al5754 aluminum material.

Material	f_N	s_N	ε_N
Al5754	0.034	0.1	0.320

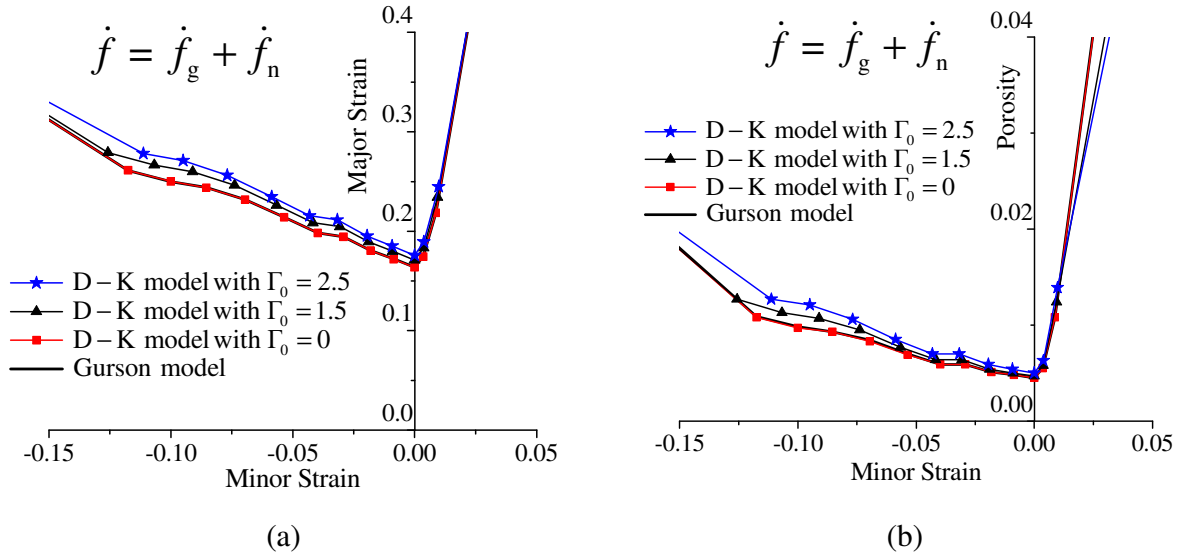


Fig. 10. (a) FLDs, and (b) porosity at localization, for Al5754 aluminum. Porosity evolution is due to growth and nucleation.

In contrast to the FLDs obtained with porosity evolution only due to growth (i.e., D-K model and Gurson model, see Fig. 8a), Fig. 10a shows that the effect of void size on strain localization is more perceptible when both growth and nucleation of porosity are considered. More specifically, as observed in Section 3.2, it is expected that smaller values of the initial non-

dimensional parameter induce rapid softening (see the stress–strain curves in Figs. 4 and 5), thereby promoting early plastic flow localization. This expectation is also confirmed by Fig. 10a, which shows that the predicted FLDs are lowered as initial non-dimensional parameter Γ_0 decreases. This trend is confirmed by Fig. 10b, which also shows the effect of the initial non-dimensional parameter on the values of porosity at localization. Note that when $\Gamma_0 = 0$, the FLD predicted by the D–K model coincides with that of the Gurson model, which is also consistent with the theoretical expectation for this particular case (i.e., the Gurson model is recovered from the D–K model when $\Gamma_0 = 0$).

In addition to growth and nucleation of voids during plastic deformation in ductile materials, coalescence of voids can also be introduced to model the rapid decay of the material stress carrying capacity. Tvergaard and Needleman [68] have modified the original Gurson model to account for the complete kinetics of voids within the material (i.e., nucleation, growth and coalescence), which corresponds to the well-known Gurson–Tvergaard–Needleman (GTN) model. Using the GTN model, the actual void volume fraction f in the expression of the yield surface is replaced by the effective porosity f^* , which accounts for the void coalescence mechanism as follows:

$$f^* = f_{\text{cr}} + \delta_{\text{GTN}}(f - f_{\text{cr}}), \quad (41)$$

where f_{cr} is the critical porosity, which marks the onset of the coalescence regime, while δ_{GTN} is the accelerating factor that governs the rapid decay of stress carrying capacity at the onset of coalescence. Note that when $f \leq f_{\text{cr}}$ (i.e., only growth and nucleation of voids are considered), the accelerating factor δ_{GTN} is set to 1, while $\delta_{\text{GTN}} > 1$ in the case of coalescence (i.e., $f > f_{\text{cr}}$). This approach, which considers the coalescence of voids beyond a critical porosity, is also used for the D–K model in what follows.

The parameters associated with the coalescence regime for the Al5754 aluminum material are reported in Table 5, while the elastic–plastic and nucleation parameters are kept the same as those used in Tables 3 and 4. The corresponding FLDs obtained with the developed approach are presented in Fig. 11a. As discussed above, coalescence causes sudden loss of the stress carrying capacity and, therefore, the hardening modulus becomes strongly negative. It has been shown in Mansouri et al. [64] that the prediction of strain localization using the Rice bifurcation criterion requires strongly negative hardening modulus in the right-hand side of the FLD (i.e., for biaxial stretching loading paths), which can be reached by considering the coalescence mechanism. Consequently, it can be observed in Fig. 11a that more localization points are obtained in the right-hand side of the FLD, as compared to the FLDs in Figs. 8a and 10a, thanks to the consideration of the void coalescence mechanism. Note that the experimental FLD, which is taken from Brunet et al. [69], is also shown in Fig. 11a for qualitative comparison.

Table 5

Coalescence parameters for the Al5754 aluminum material.

Material	f_{cr}	δ_{GTN}
Al5754	0.00284	7

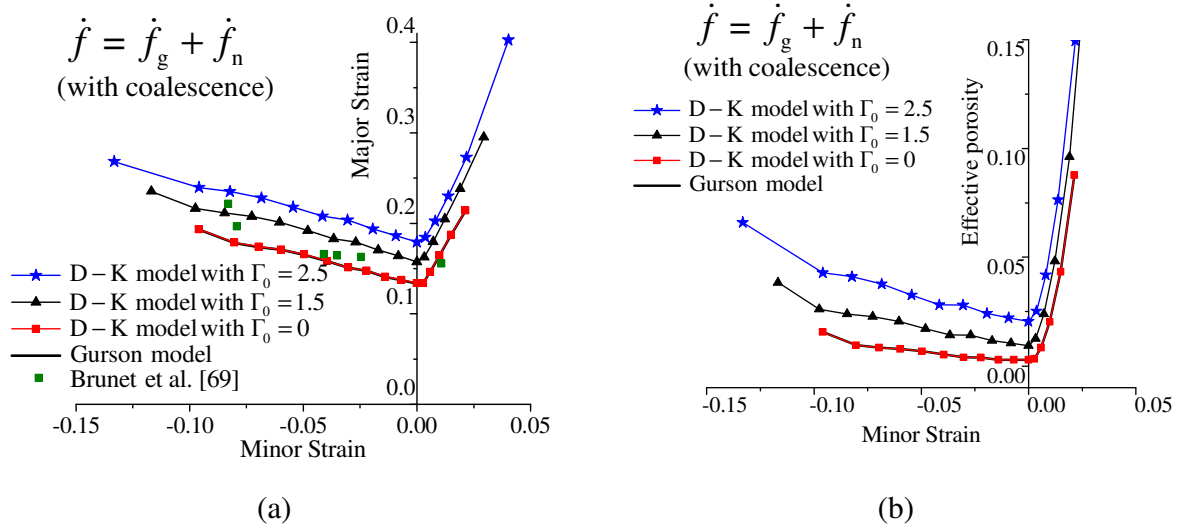


Fig. 11. (a) FLDs, and (b) effective porosity at localization, for Al5754 aluminum. Porosity evolution is due to growth, nucleation and coalescence.

Analogous to the previous FLDs, obtained using only growth and nucleation of voids, the FLDs in Fig. 11a are clearly sensitive to variation of the initial non-dimensional parameter, with lowered FLDs for smaller values of the initial non-dimensional parameter. Note also that for $\Gamma_0 = 0$, the FLD predicted by the D–K model coincides with that of the GTN model, for which the q -parameters for the void interactions are set equal to 1. Furthermore, the yield surfaces for different values of initial non-dimensional parameter are presented in Fig. 12, in which the evolution of porosity is attributed to growth, nucleation and coalescence. In contrast to Fig. 9, with porosity evolution only due to growth, Fig. 12 depicts distinct yield surfaces for different initial values of non-dimensional parameter, and for all possible values of stress triaxiality ratio, which leads in turn to a more perceptible effect on the prediction of FLDs.

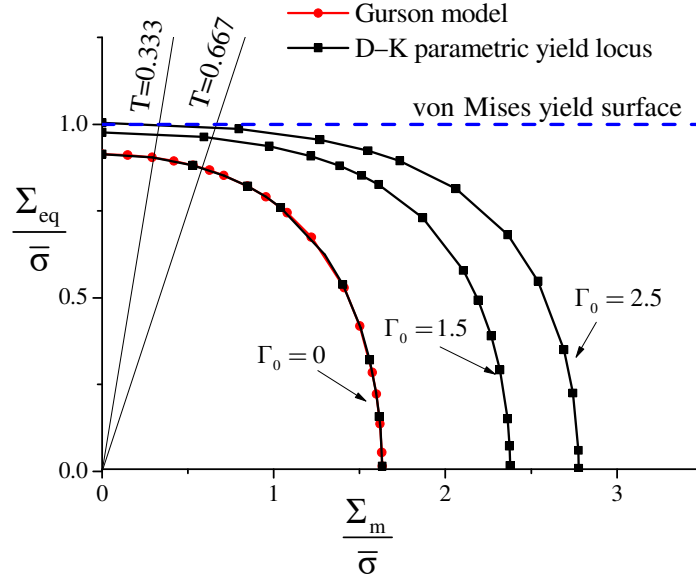


Fig. 12. Parametric yield surface for Al5754 aluminum and $\Gamma_0 = 0, 1.5$ and 2.5 . Porosity evolution is due to growth, nucleation and coalescence.

In Fig. 12, the von Mises yield surface is also illustrated. It is noteworthy that when the initial non-dimensional parameter is increased (i.e., void size is decreased), an increase in the material strength is observed (i.e., expansion of the yield surface). However, the strength of porous material cannot be larger than the strength of the sound material (i.e., undamaged material). This requires that the initial non-dimensional parameter Γ_0 must vary within a physically admissible range, i.e. $0 \leq \Gamma_0 \leq \Gamma_0^{lim}$, in which the parametric D–K yield surface must lie between the Gurson yield surface (i.e., $\Gamma_0 = 0$) and the undamaged elastic–plastic yield surface. This physical range of initial non-dimensional parameter Γ_0 can be identified by comparing the parametric D–K yield surface for various values of Γ_0 with the particular cases of Gurson yield surface (i.e., $\Gamma_0 = 0$) and von Mises yield surface (i.e., undamaged isotropic elastic–plastic model), as illustrated in the above Fig. 12. This figure reveals that the physical upper bound of the non-dimensional parameter Γ_0 is 2.5, for which the ratio between the equivalent stress and the yield stress of the fully dense matrix is lower or equal to 1 (i.e., $\frac{\Sigma_{eq}}{\bar{\sigma}} \leq 1$).

It is worth noting that the coalescence criterion used in the present model does not take the effect of void size into account. Other coalescence criteria including the effect of void size can be combined with the present approach. Among them, the constitutive model for nanoporous materials proposed by Gallican and Hure [70], in which the effect of void size on coalescence regime has been considered.

The effect of void size on the ductility limits for high initial porosity is also investigated hereafter. Note that, in the previous simulations, the initial porosity for the A15754 aluminum material has been identified by Brunet et al. [69] to a value of 0.001. To reveal the effect of void size on strain localization for larger values of initial porosity, Fig. 13 provides the FLDs predicted by the D–K model for different values of initial non-dimensional parameter, when the initial porosity is set to 0.01. The simulation results reported in Fig. 13 are obtained with the D–K model, in which the porosity evolution takes into account all three mechanisms of growth, nucleation and coalescence of voids. As previously discussed for Gurson-type models in general, and for the D–K model in particular, porosity is the most important parameter for the sensitivity of FLDs to the void size. As shown in Fig. 13, for high initial porosity (i.e., $f_0 = 0.01$), the effect of the initial non-dimensional parameter on strain localization is more significant than in the case of smaller initial porosity (i.e., $f_0 = 0.001$, see Fig. 11a). Indeed, increasing the initial non-dimensional parameter (i.e., decreasing the void size) will increase the number of voids within the material, in order to keep the same actual porosity, which will increase in turn the number of interfaces between voids and the dense matrix. Therefore, material strain hardening will be increased in this case in the same way as material ductility. This observation has also been found by Wen et al. [28], who concluded that the void size effects on material response is more significant for higher initial porosity.

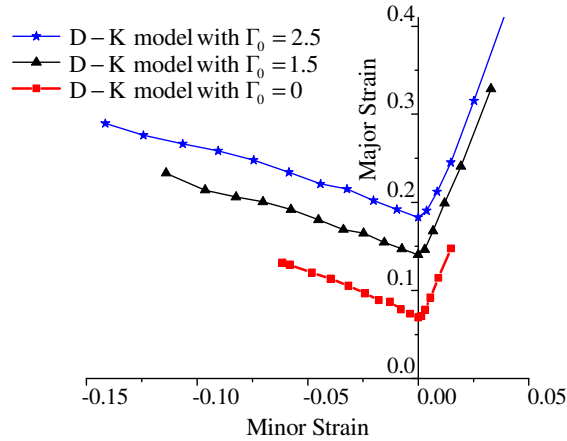


Fig. 13. FLDs for A15754 aluminum alloy with $f_0 = 0.01$. Porosity evolution is due to growth, nucleation and coalescence of voids.

5. Conclusions

In the present contribution, the phenomenological model proposed by Dormieux and Kondo [22] for ductile porous materials accounting for void size effects has been combined with the Rice bifurcation criterion to predict strain localization in thin sheet metals. The constitutive

equations have been implemented together with the Rice bifurcation criterion into the finite element code ABAQUS/Standard within the framework of large strains and fully three-dimensional approach. However, the localization bifurcation criterion has been reformulated within the plane-stress framework, as classically done for the prediction of localized necking in thin sheet metals. Linear in-plane biaxial stretching loading paths have been applied for the prediction of forming limit diagrams for the Al5754 aluminum material.

Recall that the Dormieux and Kondo [22] model, which is an extension of the original Gurson model, has been developed by performing a limit analysis for a spherical void inside a spherical RVE, and by considering a membrane with surface stresses around the void. The resulting yield function depends on the void size through a non-dimensional parameter. Considering at first only the porosity evolution due to void growth, the FLDs predicted with the present approach show no sensitivity to the void size, due to the fact that the porosity at localization remains very small. However, when successively nucleation and coalescence are considered in the evolution of porosity, FLDs exhibit more sensitivity to the void size. More specifically, it is found that the ductility limits are lowered as the initial non-dimensional parameter is decreased (i.e., when the void size is increased). In other words, decreasing the void size has a beneficial effect on formability. These findings are consistent with what has been reported in the literature regarding the void size effects on material response. Nonetheless, there is an upper bound for the initial non-dimensional parameter Γ_0 (i.e., lower bound for the void size), which is physically admissible. This upper bound, which depends on the material parameters, is identified so that the parametric D–K yield surface must lie between the Gurson yield surface and the undamaged elastic–plastic yield surface (i.e., sound material with no void). Moreover, it is found that the FLD predicted using the D–K model with an initial non-dimensional parameter $\Gamma_0 = 0$ coincides with that obtained with the Gurson model, which is also consistent with the material response for this particular case. Finally, the investigation of the combined effect of void size and initial porosity shows that smaller void sizes lead to an increase in the ductility limits, and this trend becomes more significant for high initial porosity, due to the increase of void-matrix interface strength within the material.

References

1. Keeler SP, Backofen WA. Plastic instability and fracture in sheets stretched over rigid punches. *ASM Transactions Quarterly* 1963;56(11):25-48.
2. Goodwin GM. Application of strain analysis to sheet metal forming problems in the press shop. *SAE Transactions* 1968;380-87.
3. Kachanov LM. On creep rupture time. *Izv. Acad. Nauk SSSR, Otd. Techn. Nauk* 1958;8:26-31.

4. Rabotnov YN. Creep problems in structural members. North-Holland Publishing Company 1969.
5. Lemaitre J. A Course on Damage Mechanics. Springer Science & Business Media 1992.
6. Maire JF, Chaboche JL. A new formulation of continuum damage mechanics (CDM) for composite materials. *Aerospace Science and Technology* 1997;1(4):247-57.
7. Hambli R. Comparison between Lemaitre and Gurson damage models in crack growth simulation during blanking process. *International Journal of Mechanical Sciences* 2001;43(12):2769-90.
8. Brünig M. Numerical analysis and elastic–plastic deformation behavior of anisotropically damaged solids. *International Journal of Plasticity* 2002;18(9):1237-70.
9. Menzel A, Ekh M, Runesson K, Steinmann P. A framework for multiplicative elastoplasticity with kinematic hardening coupled to anisotropic damage. *International Journal of Plasticity* 2005;21(3):397-434.
10. Besson J, Cailletaud G, Chaboche JL, Forest S. *Non-linear mechanics of materials*. Springer Science & Business Media 2009;167
11. Bouchard PO, Bourgeon L, Fayolle S, Mocellin K. An enhanced Lemaitre model formulation for materials processing damage computation. *International Journal of Material Forming* 2011;4(3):299-315.
12. Voyiadjis G. *Advances in damage mechanics: metals and metal matrix composites*. Elsevier 2012.
13. Doghri I. *Mechanics of deformable solids: linear, nonlinear, analytical and computational aspects*. Springer Science & Business Media 2013.
14. Lian J, Feng Y, Münstermann S. A modified Lemaitre damage model phenomenologically accounting for the Lode angle effect on ductile fracture. *Procedia materials science* 2014;3:1841-47.
15. Gurson AL. Continuum theory of ductile rupture by void nucleation and growth: Part I—Yield criteria and flow rules for porous ductile media. *Journal of Engineering Materials and Technology* 1977;99(1):2-15.
16. Gologanu M, Leblond JB, Devaux J. Approximate models for ductile metals containing non-spherical voids—case of axisymmetric prolate ellipsoidal cavities. *Journal of the Mechanics and Physics of Solids* 1993;41(11):1723-54.
17. Gologanu M, Leblond JB, Devaux J. Approximate models for ductile metals containing nonspherical voids—case of axisymmetric oblate ellipsoidal cavities. *Journal of Engineering Materials and Technology* 1994;116(3):290-97.
18. Madou K, Leblond JB. A Gurson-type criterion for porous ductile solids containing arbitrary ellipsoidal voids—I: Limit-analysis of some representative cell. *Journal of the Mechanics and Physics of Solids* 2012;60(5):1020-36.

19. Madou K, Leblond JB. A Gurson-type criterion for porous ductile solids containing arbitrary ellipsoidal voids—II: Determination of yield criterion parameters. *Journal of the Mechanics and Physics of Solids* 2012;60(5):1037-58.
20. Madou K, Leblond JB. Numerical studies of porous ductile materials containing arbitrary ellipsoidal voids—I: Yield surfaces of representative cells. *European Journal of Mechanics-A/Solids* 2013;42:480-89.
21. Madou K, Leblond JB, Morin L. Numerical studies of porous ductile materials containing arbitrary ellipsoidal voids—II: Evolution of the length and orientation of the void axes. *European Journal of Mechanics-A/Solids* 2013;42:490-507.
22. Dormieux L, Kondo D. An extension of Gurson model incorporating interface stresses effects. *International Journal of Engineering Science* 2010;48(6):575-81.
23. Monchiet V, Bonnet G. A Gurson-type model accounting for void size effects. *International Journal of Solids and Structures* 2013;50(2):320-27.
24. Morin L, Kondo D, Leblond JB. Numerical assessment, implementation and application of an extended Gurson model accounting for void size effects. *European Journal of Mechanics-A/Solids* 2015;51:183-92.
25. Lacroix R, Leblond JB, Perrin G. Numerical study and theoretical modelling of void growth in porous ductile materials subjected to cyclic loadings. *European Journal of Mechanics-A/Solids* 2016;55:100-09.
26. Morin L, Michel JC, Leblond JB. A Gurson-type layer model for ductile porous solids with isotropic and kinematic hardening. *International Journal of Solids and Structures* 2017;118:167-78.
27. Hutchinson JW. Plasticity at the micron scale. *International Journal of Solids and Structures* 2000;37(1-2):225-38.
28. Wen J, Huang Y, Hwang KC, Liu C, Li M. The modified Gurson model accounting for the void size effect. *International Journal of Plasticity* 2005;21(2):381-95.
29. Fleck NA, Muller GM, Ashby MF, Hutchinson JW. Strain gradient plasticity: theory and experiment. *Acta Metallurgica et Materialia* 1994;42(2):475-87.
30. Schlu N, Grimpe F, Bleck W, Dahl W. Modelling of the damage in ductile steels. *Computational Materials Science* 1996;7(1-2):27-33.
31. Begley MR, Hutchinson JW. The mechanics of size-dependent indentation. *Journal of the Mechanics and Physics of Solids* 1998;46(10):2049-68.
32. Nix WD, Gao H. Indentation size effects in crystalline materials: a law for strain gradient plasticity. *Journal of the Mechanics and Physics of Solids* 1998;46(3):411-25.
33. Stölken JS, Evans AG. A microbend test method for measuring the plasticity length scale. *Acta Materialia* 1998;46(14):5109-15.
34. Kawasaki M, Xu C, Langdon TG. An investigation of cavity growth in a superplastic aluminum alloy processed by ECAP. *Acta Materialia* 2005;53(20):5353-64.

35. Khraishi TA, Khaleel MA, Zbib HM. A parametric-experimental study of void growth in superplastic deformation. *International Journal of Plasticity* 2001;17(3):297-315.
36. Fu MW, Chan WL. Geometry and grain size effects on the fracture behavior of sheet metal in micro-scale plastic deformation. *Materials & Design* 2011;32(10):4738-46.
37. Chentouf SM, Belhadj T, Bombardier N, Brodusch N, Gauvin R, Jahazi M. Influence of predeformation on microstructure evolution of superplastically formed Al 5083 alloy. *The International Journal of Advanced Manufacturing Technology* 2017;88(9-12):2929-37.
38. Li S, Jin S, Huang Z. Cavity Behavior of Fine-Grained 5A70 Aluminum Alloy during Superplastic Formation. *Metals* 2018;8(12):1065.
39. Liu B, Qiu X, Huang Y, Hwang KC, Li M, Liu C. The size effect on void growth in ductile materials. *Journal of the Mechanics and Physics of Solids*. 2003;51(7):1171-87.
40. Brach S, Dormieux L, Kondo D, Vairo G. A computational insight into void-size effects on strength properties of nanoporous materials. *Mechanics of Materials* 2016;101:102-17.
41. Biener J, Hodge AM, Hamza AV, Hsiung LM, Satcher Jr JH. Nanoporous Au: A high yield strength material. *Journal of Applied Physics* 2005;97(2):024301.
42. Biener J, Hodge AM, Hayes JR, Volkert CA, Zepeda-Ruiz LA, Hamza AV, Abraham FF. Size effects on the mechanical behavior of nanoporous Au. *Nano Letters* 2006;6(10):2379-82.
43. Hakamada M, Mabuchi M. Mechanical strength of nanoporous gold fabricated by dealloying. *Scripta Materialia* 2007;56(11):1003-06.
44. Mi C, Buttry DA, Sharma P, Kouris DA. Atomistic insights into dislocation-based mechanisms of void growth and coalescence. *Journal of the Mechanics and Physics of Solids* 2011;59(9):1858-71.
45. Xu ZT, Peng LF, Fu MW, Lai XM. Size effect affected formability of sheet metals in micro/meso scale plastic deformation: experiment and modeling. *International Journal of Plasticity* 2015;68:34-54.
46. Xu ZT, Peng LF, Lai XM, Fu MW. Geometry and grain size effects on the forming limit of sheet metals in micro-scaled plastic deformation. *Materials Science and Engineering: A* 2014;611:345-53.
47. Xu Z, Peng L, Yi P, Lai X. An investigation on the formability of sheet metals in the micro/meso scale hydroforming process. *International Journal of Mechanical Sciences* 2019;150:265-76.
48. Dormieux L, Kondo D. Non linear homogenization approach of strength of nanoporous materials with interface effects. *International Journal of Engineering Science* 2013;71:102-10.
49. Brach S, Dormieux L, Kondo D, Vairo G. Strength properties of nanoporous materials: a 3-layered based non-linear homogenization approach with interface effects. *International Journal of Engineering Science* 2017;115:28-42.

50. Considère M. Memoire sur l'emploi du fer et de l'acier dans les constructions. *Ann. Ponts et Chaussées* 1885;9:574–775.
51. Swift H. Plastic instability under plane stress. *Journal of the Mechanics and Physics of Solids* 1952;1(1):1-18.
52. Hill R. On discontinuous plastic states, with special reference to localized necking in thin sheets. *Journal of the Mechanics and Physics of Solids* 1952;1(1):19-30.
53. Hora P, Tong L, Reissner J. A prediction method for ductile sheet metal failure in FE-simulation. In *Proceedings of NUMISHEET* 1996;96:252-56.
54. Marciniak Z, Kuczyński K. Limit strains in the processes of stretch-forming sheet metal. *International Journal of Mechanical Sciences* 1967;9(9):609-20.
55. Hill R. A general theory of uniqueness and stability in elastic-plastic solids. *Journal of the Mechanics and Physics of Solids* 1958;6(3):236-49.
56. Valanis KC. Banding and stability in plastic materials. *Acta Mechanica* 1989;79(1-2):113-41.
57. Rudnicki JW, Rice JR. Conditions for the localization of deformation in pressure-sensitive dilatant materials. *Journal of the Mechanics and Physics of Solids* 1975;23(6):371-94.
58. Rice JR. Localization of plastic deformation. In: Koiter (Ed.), *Theoretical and Applied Mechanics* 1976;1:207-20.
59. Bigoni D, Hueckel T. Uniqueness and localization—I. Associative and non-associative elastoplasticity. *International Journal of Solids and Structures* 1991;28(2):197-213.
60. Neilsen MK, Schreyer HL. Bifurcations in elastic-plastic materials. *International Journal of Solids and Structures* 1993;30(4):521-44.
61. Volk W, Hora P. New algorithm for a robust user-independent evaluation of beginning instability for the experimental FLC determination. *International Journal of Material Forming* 2011;4(3):339-46.
62. Situ Q, Jain MK, Bruhis M. A suitable criterion for precise determination of incipient necking in sheet materials. In *Materials Science Forum* 2006;519:111-16.
63. Narasimhan K, Wagoner RH. Finite element modeling simulation of in-plane forming limit diagrams of sheets containing finite defects. *Metallurgical Transactions A* 1991;22(11):2655-65.
64. Mansouri LZ, Chalal H, Abed-Meraim F. Ductility limit prediction using a GTN damage model coupled with localization bifurcation analysis. *Mechanics of Materials* 2014;76:64-92.
65. Chalal H, Abed-Meraim F. Hardening effects on strain localization predictions in porous ductile materials using the bifurcation approach. *Mechanics of Materials* 2015;91:152-66.
66. Tvergaard V. Effect of yield surface curvature and void nucleation on plastic flow localization. *Journal of the Mechanics and Physics of Solids* 1987;35(1):43-60.

67. Chu CC, Needleman A. Void nucleation effects in biaxially stretched sheets. *Journal of Engineering Materials and Technology* 1980;102(3):249-56.
68. Tvergaard V, Needleman A. Analysis of the cup-cone fracture in a round tensile bar. *Acta Metallurgica* 1984;32(1):157-69.
69. Brunet M, Mguil S, Morestin F. Analytical and experimental studies of necking in sheet metal forming processes. *Journal of Materials Processing Technology* 1998;80:40-46.
70. Gallican V, Hure J. Anisotropic coalescence criterion for nanoporous materials. *Journal of the Mechanics and Physics of Solids*. 2017;108:30-48.